Check for updates

Advanced Materials Technologies

ADVANCED MATERIALS TECHNOLOGIES
www.advmattechnol.com

SPECIAL ISSUE Flexible, Stretchable and Printable Electronic Materials for Sustainable Healthcare, Sensing and Actuation, Energy Applications and Interconnections

RESEARCH ARTICLE OPEN ACCESS

Overcoming Printing and Interfacial Challenges in Liquid Metal Direct Writing for Integrated Stretchable Electronics

Maximilian Krack[1,2] | Lennert Purnal[1,2] | Parth Vinayakrao Sewlikar[3] | Sam Cuyvers[1,2] | Gus Geurts[1,2] | Rathul Nengminza Sangma[4] | Derese Desta[1,2] | Dieter Reenaers[1,2] | Bart Ruttens[1,2] | Iris De Graeve[3] | Tom Hauffman[3] | Seppe Terryn[3,4] | Bram Vanderborght[4] | Michaël Daenen[1,2] | Wim Deferme[1,2] | Monika Rai[1,2]

[1]Hasselt University, Institute for Materials Research, Hasselt, Belgium | [2]IMEC vzw, division IMOMEC, Diepenbeek, Belgium | [3]Materials and Chemistry, Sustainable Materials Engineering, Vrije Universiteit Brussel, Elsene, Belgium | [4]Brubotics, Vrije Universiteit Brussel and IMEC, Elsene, Belgium

Correspondence: Maximilian Krack (max.krack@uhasselt.be)

Received: 23 September 2025 | **Revised:** 15 November 2025 | **Accepted:** 1 December 2025

Keywords: direct writing | liquid metal | stretchable electronics

ABSTRACT

Direct writing enables rapid prototyping of liquid metal-based stretchable electronics. Challenges, such as printing on uneven surfaces, a limited understanding of the flow behavior, and interfacial issues between liquid metal and electronic terminals for reliable interconnections, remain. We innovatively utilize the kinematic bed of a 3D printer to dynamically control the stand-off distance during direct writing. This enables reliable printing on irregular surfaces and 3D structures with slopes up to 10%. We discover that the thickness of printed liquid metal is affected by a pressure-driven backflow, enabling tuning of thickness in a range of 100 μm. To solve interfacial challenges, we develop a novel solder-based technique that forms a liquid metal interface on metal coatings, resulting in 100% print reliability between the LM meniscus and the electronic terminal. This interface reduces contact resistance by a factor of four, and improves electrical stability during cyclic strain, with negligible resistance change up to three million cycles. These innovations are demonstrated through the fabrication of large (order of ≥10 cm) stretchable devices, and stretchable devices featuring integrated electronic components. Our contributions address the limitations of direct writing of liquid metal, advancing the practical realization of reliable, scalable, and fully integrated stretchable electronic systems.

1 | Introduction

Recent advances in flexible and stretchable electronics combine skin conformity and durability, enabling emerging applications where rigid electronics fall short, such as soft robotic grippers and on-skin devices [1–8]. To realize these systems, electrical interconnections must conduct reliably under strain. Conductive composites, serpentine metals, and gallium-based liquid metals (LMs) have all been explored [9–14]. Galinstan, a gallium–indium–tin alloy, offers high conductivity (3.46×10^6 S m^{-1}) and a low melting point (10–11°C). The alloy adheres onto smooth surfaces and can be patterned into various forms due to its stabilizing oxide skin [9, 15, 16].

LMs are typically patterned onto elastomers and encapsulated, allowing the conductor to deform with the substrate [17–21]. Patterning methods, among others, include microchannel injection, stencil-assisted spray deposition, and direct writing [22–28]. Direct writing (DW) stands out for its digital control, high resolution (down to ≈2 μm), and design flexibility. DW is a challenging technique that uses a meniscus at the nozzle tip generated under constant pressure. The oxide adheres to the substrate, and motion

This is an open access article under the terms of the Creative Commons Attribution-NonCommercial-NoDerivs License, which permits use and distribution in any medium, provided the original work is properly cited, the use is non-commercial and no modifications or adaptations are made.
© 2025 The Author(s). *Advanced Materials Technologies* published by Wiley-VCH GmbH

shears the LM from the nozzle, similar to a ballpoint pen. The main challenges of DW include printing on non-flat (large-area) substrates and interfacial problems, particularly with electronic terminals, which negatively affect the scalability, integrateability, interfacing, and applications of the technique [29, 30].

The distance between the nozzle and the substrate is defined as stand-off distance (SOD). The SOD must be maintained within a few micrometers for reliable printing. This becomes especially difficult for non-planar substrates, where minor surface variations can interrupt printing. While spin-coated elastomers or wafers are commonly used for their flatness [30–32], these materials and techniques are less compatible with scalable production. To solve this persistent problem, we adapt and utilize a technology that is used in the commercial 3D-printing space in an innovative way. This technology consists of a BLTouch sensor for surface height mapping and a kinematic bed that can dynamically compensate for surface irregularities. The printed traces are then characterized for printability and reproducibility, where we discover that a pressure-driven flow affects the thickness of the traces during printing. We clearly elaborate this phenomenon, building on existing literature reporting that LM is mainly pulled from the nozzle and showing that this can be used to control trace thickness [26, 29, 30, 33].

Further, integrating electronic components into liquid metal-based stretchable electronics (LMSE) provides several benefits and is an important step toward integrated stretchable electronics. These benefits include adding functionality to the device, such as sensors, and reducing the need for dangling external electronics, which simplifies wiring and assembly. Among the materials for electronic terminals, ENIG (electroless nickel immersion gold) shows the most consistent long-term stability with LM and is used most throughout this work [32]. In DW, interfacial behavior plays a central role and must be considered in two distinct ways: adhesion and wetting [34]. Adhesion is governed by the contact of the LM oxide skin with the surface. Smooth, hydrophilic elastomers generally provide reliable adhesion through solid–solid contact with the oxide, whereas metallic electronic terminals do not. Wetting, in contrast, is favorable on metals and requires the removal of the oxide so that pristine LM can directly contact the electric terminals to form stable electrical interconnections [34]. A persistent limitation of DW is therefore the poor adhesion between the oxide and commercial coatings, combined with insufficient LM wetting to achieve a sufficient mechanical contact area. These two issues, unreliable printing and high contact resistance, have limited the integration of bulk electronic components into LMSE via DW. We overcome interfacial challenges between LM and ENIG by introducing an LM interface layer fabricated using a novel scalable solder-priming (SP) technique, which leverages an electronic terminal wetted with LM prior to the printing. We examine the long-term stability of this interface and its suitability for integrated soft devices.

Our work advances liquid metal direct writing by providing solutions for core challenges. These include printing on irregular large-area surfaces with a kinematic print bed, understanding the flow behavior during printing for more predictable process windows, and a solder priming method applied to the electronic terminals that solves interfacial issues and improves the performance of fabricated stretchable electronics. The technical innovations are demonstrated with relevant applications: A long cable (25 cm), a 16 LED array and an integrated wearable sensor. We believe that these improvements support the broader adoption of direct writing as a platform for the manufacturing of scalable and integrated stretchable electronics.

2 | Results and Discussion

2.1 | Liquid Metal Direct Writing Challenges

This section provides an overview of the major challenges associated with DW of LM and introduces our key innovations to overcome them. Our DW platform is based on a commercially available 3D printer equipped with a kinematic bed and a high-precision dispenser (Figure S1). The high precision dispenser is necessary to avoid dispensing spherical droplets that would ruin the printed traces (Figure S2). The motions of the system, including bed mesh compensation, is controlled via open-source Klipper firmware. Fabrication of stretchable devices builds on our previously reported scalable process, detailed further in the Experimental Section [35]. The overall process for DW LMSE with integrated electronic components is schematized in Figure 1 and consists of the following three key steps:

1. Print start: The primed nozzle lowers to make initial contact with the substrate or component.
2. Printing: The nozzle traverses the surface while the meniscus shears and extrudes LM.
3. Print end: Shearing across the electronic terminal, and the nozzle is lifted from the substrate or component.

The print start is especially critical, as it defines the first contact between the LM oxide and the surface. Strong affinity between the LM and the surface is essential [36]. Generally, oxide rupture happens during the shearing motion. However, the poor adhesion between the LM oxide and the electronic terminal prevents sufficient shearing, resulting in poor or non-functional interconnections. A workaround involves an additional printing step as introduced by Kim et al. [32]. Rather than initiating the print on the electronic terminal, the print starts on the stretchable substrate and then transitions onto the electronic terminal. However, the extra step complicates the printing process and introduces LM "blobs" between the printed traces, which can uncontrollably grow (Figure S2). To resolve this, we introduce a thin LM interface formed via a new solder priming method, applied directly to the ENIG surface as shown in Figure 1. This interfacial layer fully wets the electronic terminal before the print, drastically improving printability and the interconnection quality. A detailed discussion of this method and its full benefits is provided in Figure 4.

During the printing phase, maintaining a constant SOD is crucial. Even micrometer-scale deviations can drastically alter line geometry or break continuity. Naturally, the larger the substrate, the more prevalent the surface inhomogeneities. This process critically depends on precise control of both syringe pressure and the SOD. The kinematic bed of the RatRig printer dynamically compensates for uneven surface meshes probed with a BLTouch

2365709x, 2026, 15, Downloaded from https://advanced.onlinelibrary.wiley.com/doi/10.1002/admt.202502023 by IMEC Library - IMEC , Wiley Online Library on [19/11/2026]. See the Terms and Conditions (https://onlinelibrary.wiley.com/terms-and-conditions) on Wiley Online Library for rules of use; OA articles are governed by the applicable Creative Commons License

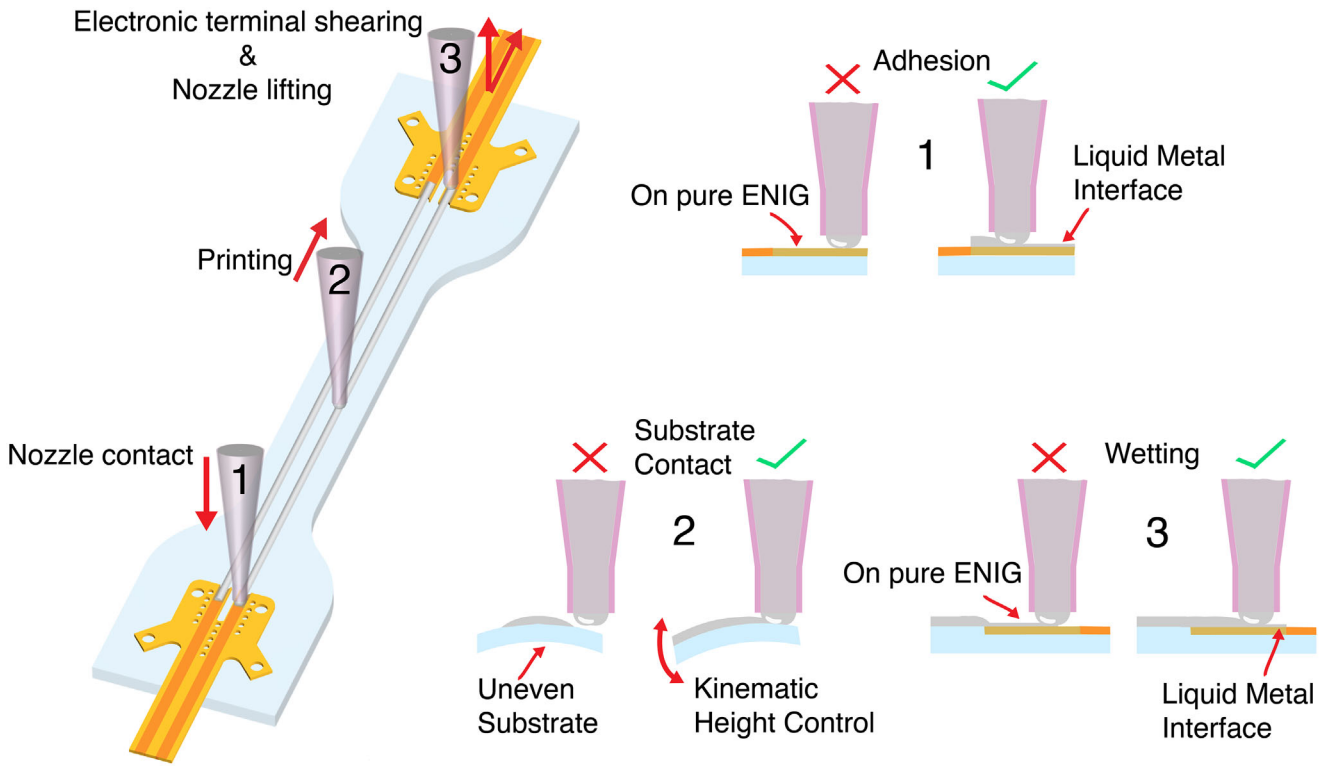


FIGURE 1 | The figure shows a simplified schematic of the DIW process. The schematic highlights challenges and solutions that are proposed in this paper. 1) It is difficult due to adhesion issues to print on common electrode coatings such as ENIG, especially in the first step. This is solved with a LM interface layer. 2) The nozzle meniscus can lose contact with the substrate on uneven surfaces. This is solved with a kinematic printing bed that utilities a bed mesh of the surface recorded with a BLTouch probe sensor. 3) When lifting the nozzle, LM will spill if the pressure is too high. With dynamic pressure control, it can be lowered during nozzle lifting.

probe by adjusting height in real-time. This allows us to replace spin-coated, ultra-flat substrates with more scalable substrate preparation techniques [30–32].

The print end poses another interfacial challenge: The oxide is now breaking because of the shearing motion, and the LM can wet the electronic terminal. However, the resulting contact area between the LM and the terminal is low due to insufficient wetting, which leads to a high contact resistance that can reduce device performance [29]. The SP solves this challenge too as the electronic terminal is already fully wet during the printing. We additionally implement a dynamic pressure control to prevent LM spilling when the nozzle is lifted (Figure S1).

The following sections provide a more in-depth discussion of these innovations and how they improve the overall performance and reliability of the direct writing process.

2.2 | Direct Writing on Uneven Surfaces

While the direct writing of LM is decently well understood and proven to be reliable across a wide parameter space on ultra-flat substrates [30], printing on uneven or tilted surfaces remains a major challenge. On such substrates, surface height variations in the micrometer range influence the meniscus–substrate interaction. This proportionally influences line geometry, and can even lead to fully broken lines when the SOD moves out of the printable range (≥ 220 µm, dependent on multiple parameters) as demonstrated in previous work [30]. To address this, we utilize a BLTouch probe sensor in combination with a kinematic print bed to dynamically compensate for substrate irregularities. To generate a bed mesh via Klipper firmware, the system probes the surface of the substrate in a defined grid array relative to an initial homing point. The bed mesh can then be loaded by the system before the start of the print. However, applying this technique to soft substrates is non-trivial and, to the best of our knowledge, has not been previously demonstrated. The BLTouch probe itself weighs less than 3 g and exerts negligible force on rigid substrates. On soft substrates, this force can cause slight indentation, resulting in a negative offset in the bed mesh. Notably, this indentation effect depends on the substrate thickness. The aim is therefore to create a FEM model with COMSOL to reliably predict the probe indentation for substrates of any material with varying thickness to accurately apply the bed mesh during print.

First, we evaluate whether the BLTouch probe maintains acceptable accuracy on soft substrates via the *PROBE ACCURACY* command of Klipper. On hard surfaces, the probe's tolerance is below 0.5 µm. On soft Ecoflex surfaces, this increases to 3 µm, still well within acceptable limits for LM direct writing. The results of the COMSOL simulations of probe indentation are shown in Figure 2a. We used Ecoflex 30 (very soft) and Dragon Skin 10 (stiffer) as representative materials and modeled them using hyperelastic Mooney–Rivlin parameters extracted from

2365709x, 2026, 15, Downloaded from https://advanced.onlinelibrary.wiley.com/doi/10.1002/admt.202502023 by IMEC Library - IMEC , Wiley Online Library on [19/11/2026]. See the Terms and Conditions (https://onlinelibrary.wiley.com/terms-and-conditions) on Wiley Online Library for rules of use; OA articles are governed by the applicable Creative Commons License

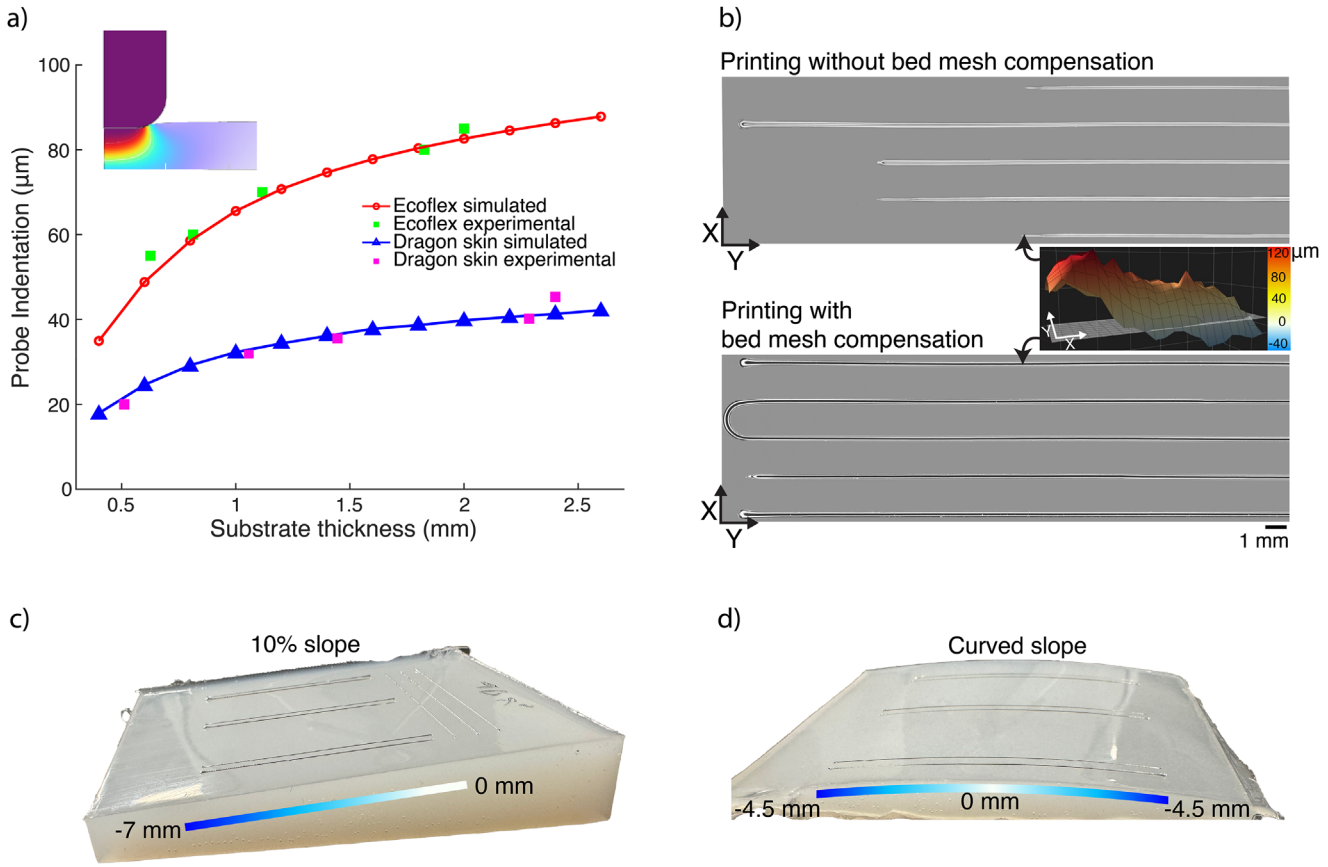


FIGURE 2 | (a) COMSOL simulation of a probe indentation into a soft surface with variable thickness. The probe indents deeper into a softer and thicker surface, which increases the z-offset that needs to be applied to the system. (b) Test structures printed on the same substrate which was probed to generate a bed mesh. Traces printed without bed mesh compensation disconnect and appear inhomogeneous as the SOD is not controlled, while traces are printing fine with bed mesh compensation. (c) and (d) demonstrate advanced capabilities of the bed mesh compensation, where (c) the LM is printed on a 10% sloped Ecoflex substrate, and (d) is printed on a curved slope.

uniaxial tensile tests (Figure S3). The force of the probe during indentation for the model was measured with a force sensor and is approximately 11 mN. The simulation shows that indentation depth is greater on softer substrates and decreases with reduced thickness. For instance, a 2 mm thick Ecoflex substrate requires a Z-offset correction of 90 µm. Experimental validation was performed by homing onto substrates of different thicknesses and incrementally increasing the nozzle height until the dent caused by the probe was no longer visible. The experimental results fit well with the simulated curve as seen in Figure 2a. Therefore, this approach allows for an accurate approximation of the indentation offset during bed meshing.

Next, we evaluated whether the kinematic bed compensation enables reliable LM printing on uneven surfaces. To test this, we printed 40 mm long parallel line patterns onto square 2 mm thick injection molded Ecoflex 30 substrates with a length and depth of 140 and 50 mm, respectively. The printing parameters are a pressure of 1.6 kPa, printing velocity of 6.5 mm s^{-1}, and a SOD of 0.18 mm (more detailed discussed in the experimental section). Bed meshing time depends on the substrate's size and print complexity, ranging from 30 s to 15 min. In the case of the 140 × 50 mm substrate and straight LM lines, meshing took 2 min. Figure 2b compares the parallel lines printed without and with bed mesh compensation. The mesh map reveals that the substrate exhibits tilt and multidirectional height inhomogeneities up to 160 µm relative to the homing point (edge of substrate), which is generally the range for a substrate of this size. Without bed mesh compensation, the height irregularities translate directly to the SOD, causing irregular geometry, and full lines to disconnect as seen in the image. The disconnecting lines are caused by the areas with negative offset where the meniscus moves too far away from the substrate. With bed mesh compensation enabled, the LM traces print reliably and uniformly, eliminating the need for ultra-flat substrates often used in literature. With our process parameters and bed mesh compensation enabled, the SOD can vary from 20 to 250 µm within the effective pressure range of 0.85–1.85 kPa to print patterns.

To further demonstrate the capabilities of this approach, we printed straight lines on substrates with a controlled and reproducible slope and curvature. As shown in Figure 2c, our system can reliably print on a 10% incline, which translates to a vertical change of 100 µm per millimeter. Although even steeper angles are possible for the kinematic bed to compensate, they would require angled nozzles rather than flat ones [27]. Without bed mesh compensation, we observed that the nozzle would move easily outside of the previously established range of 250 µm printing downwards, or push into the substrate moving upwards. Figure 2d shows successful printing across a curved surface,

2365709x, 2026, 15, Downloaded from https://advanced.onlinelibrary.wiley.com/doi/10.1002/admt.202502023 by IMEC Library - IMEC , Wiley Online Library on [19/11/2026]. See the Terms and Conditions (https://onlinelibrary.wiley.com/terms-and-conditions) on Wiley Online Library for rules of use; OA articles are governed by the applicable Creative Commons License

highlighting the ability of the kinematic bed to rapidly compensate for a change in the sloped surface. These capabilities go beyond simple flatness correction and suggest exciting opportunities for printing on complex 3D geometries. We speculate that future implementations of this approach will enable LM printing directly onto fully 3D structures.

2.3 | Liquid Metal Flow Behavior during Direct Writing

We systematically characterize the geometry of the LM lines that we printed on the previously described injection molded substrates using the bed mesh compensation (Figure S4). Additionally, to demonstrate that the kinematic bed compensation can be reliably scaled down, we printed traces with a smaller nozzle (id = 0.25 mm). We achieve a reliable range of 100–400 µm in trace width which makes the technique compatible with a large fraction of pitch sizes of conventional SMDs. The variability of the printed traces remains within 5% of the average line width and thickness in the optimized parameter range as previously investigated with spin coated substrates [30]. This demonstrates that bed mesh compensation is working accurately at the micrometer scale, and that ultra-flat substrates are no longer required to achieve high print reliability. In the printed traces we observe the characteristic width inflection behavior extensively described in the literature (Figure S4)[30]. Simultaneously, we noted a non-linear relationship between SOD and trace thickness, with printed traces often being thicker than the SOD itself (Figure S4). This observation prompted a deeper investigation into the factors influencing trace thickness, an underexplored and challenging aspect of DW. The goal here is to improve understanding of the technique and to better predict printing outcomes.

Existing literature reports that the thickness of LM traces depends on the amount of LM sheared or "pulled" from the nozzle tip [26, 29, 30, 33]. Our findings suggest that the applied pressure plays a secondary - but crucial - role regarding trace thickness. As shown in Figure 3a, we measured trace thickness and width at a constant velocity of 6.6 mm s^{-1} for SODs of 60 µm and 120 µm (id = 0.56 mm). At 120 µm, increasing pressure leads to a wider contact area between the meniscus and the substrate, resulting in both increased width and thickness. However, at 60 µm, the width

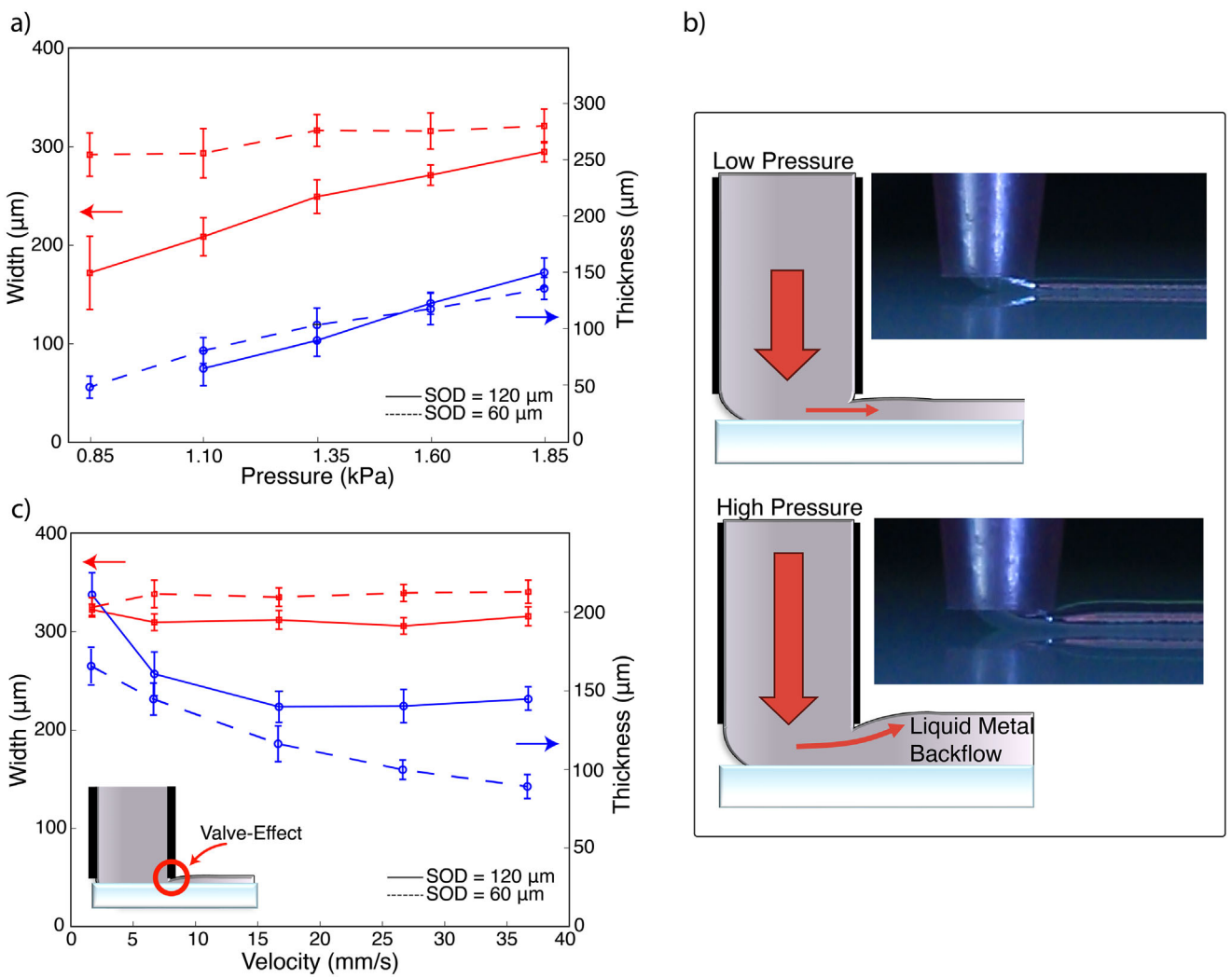


FIGURE 3 | (a) Width and thickness of printed LM deposited at different pressure and SOD values. (b) Photograph and sketch of the LM printing at a pressure difference of 1 kPa. (c) Width and thickness of printed LM deposited at different velocities and SOD values.

2365709x, 2026, 15, Downloaded from https://advanced.onlinelibrary.wiley.com/doi/10.1002/admt.202502023 by IMEC Library - IMEC , Wiley Online Library on [19/11/2026]. See the Terms and Conditions (https://onlinelibrary.wiley.com/terms-and-conditions) on Wiley Online Library for rules of use; OA articles are governed by the applicable Creative Commons License

remains nearly constant across all pressures, suggesting the full meniscus circumference is already in contact with the surface. Yet, the thickness still increases at a rate similar to that observed at 120 μm, indicating that excess LM is backflowing into the printed trace, expanding it vertically while the lateral footprint remains pinned. The maximum change in thickness is 100 μm observed at the highest pressure difference of 1 kPa.

To directly visualize this behavior, we recorded the printing process using a macro lens at a SOD of 120 μm (Video S1). Figure 3b shows still images from the video. At low pressure (0.85 kPa), the LM is cleanly pulled from the nozzle, forming a thin trace. As the pressure increases to 1.85 kPa, the LM begins to flow backward beyond the physical confines of the nozzle tip, thickening the trace. During printing, the continuous shearing of the meniscus breaks the oxide layer and opens a pathway for LM to flow. The flow rate is governed by the pressure difference ΔP between the pressure at the nozzle tip and the internal pressure of the trace [37].

At an SOD of 60 μm, below the width inflection point, the contact angle of the trace is less than 90° (Figure S4) [30]. Under this assumption, the internal pressure P_i of the printed trace can be approximated using the Young–Laplace equation:

$$P_i = \frac{\gamma}{R} = \frac{\gamma}{\frac{t}{2} + \frac{w^2}{8t}} \quad (1)$$

here, γ is the effective surface tension of Galinstan (535 mN m^{-1}), R is the radius of curvature, w is the trace width, and t is the trace thickness [9, 30, 38]. Using this model, we calculate that the internal pressure difference between traces printed at 1.85 and 0.85 kPa is approximately 1 kPa. This supports the hypothesis that the applied pressure drives LM back into the trace, increasing its thickness.

To further explore the dynamics of backflow, we varied the printing velocity while maintaining a constant pressure of 1.6 kPa, using both 60 μm and 120 μm SODs. As shown in Figure 3c, trace width remains unaffected by velocity, confirming that the contact line is set by the initial meniscus–substrate interaction. In contrast, trace thickness decreases with increasing velocity, as faster printing reduces the time available for LM to backflow. At 120 μm SOD, the thickness stabilizes once velocities exceed 15 mm s^{-1}, whereas at 60 μm SOD, the thickness continues to decline up to 40 mm s^{-1}. Beyond 40 mm s^{-1}, vibration effects increasingly distort the trace geometry; therefore this data is not considered (Figure S5). These observations can be explained by considering the pressure difference driving backflow, ΔP, which decreases as the internal pressure of the printed trace rises [37]. Because trace width remains fixed, the radius of curvature is primarily determined by thickness. According then to Young-Laplace, thinner traces exhibit higher curvature, leading to lower internal pressure and thus promoting faster backflow. This produces a self-stabilizing mechanism: the trace thickness increases until it reaches a critical value of approximately 140 μm, beyond which further velocity-increase only marginally reduce thickness. An exception occurs at a SOD of 60 μm, where the thickness continues to decrease. The nozzle edge functions as a mechanical valve that restricts backflow and amplifies the effect of velocity. Additionally, capillary forces become more dominant at such small gaps, further restricting fluid flow.

Understanding the coupling between printing parameters and backflow dynamics advances DW by enabling more predictable and reliable process windows. The next step toward further advancing the technology is to overcome the interfacial challenges that arise when printing on electronic terminals.

2.4 | Solder Priming

LMSE require reliable connections to external electronics via flexible PCBs or internal functional components such as resistors. Achieving this remains a major challenge due to the interfacial issues between LM and electronic terminals that emerge during printing.

To address this limitation, we developed a novel method that greatly improves printability on metallic coatings by forming an interfacial LM layer through conventional scalable soldering prior to the printing. We name this method "Solder Priming", as it is a pretreatment process that creates an interfacial layer that promotes adhesion and wetting of the LM. The process is illustrated in Figure 4a (Video S2). First, a small amount of commercial solder flux is applied to the metallic coating. Second, ≤ 3 μL of LM is deposited. Third, the LM is heated using a 350°C soldering iron. In less than a second, the LM spontaneously wets the coating. Similar to conventional soldering, the flux most likely removes surface oxides, both from the LM and the metallic coating. Without the oxide, LM fully wets the electronic terminal, enabling direct metal–metal contact and improved interconnection. We found the high temperature of 350°C to be critical to initiate the wetting. With lower temperatures (even 300°C), we observed that the LM would form non-wetting droplets. Finally, excess LM is removed with a syringe and the area is rinsed with isopropanol. This SP technique is compatible with various other metals commonly used in SMD components, namely silver (Ag), tin (Sn), copper (Cu), and (pure) gold (Au) (Figure S6). Additionally, the SP is tested on a more heat sensitive flexible polyethylene terephthalate (PET) substrate with the same ENIG terminals. The substrate does not show any visible damage such as melting, burning and deformation during the treatment (t = 1 s) at 350°C.

In Figure 4b, scanning electron microscopy (SEM) images of the ENIG terminals are compared. The first image shows pure ENIG, in the second image, LM was forcefully spread (to break the oxide) on ENIG, and excess was removed with a syringe, and the third image shows a SP electronic terminal. Forceful spreading is not sufficient to achieve uniform coverage, which is clear from the second image. In the SP electronic terminal, the LM covers the full area. Further, interfacial forces are strong enough that the SP electronic terminal remains covered with LM even after pipetting. Noticeable dark spots are visible in the SP image, and EDX analysis at two spots was carried out to relatively compare the elemental distributions of the spots (Figure S7). The spectra show that the dark spots consist mostly of carbon and oxygen, which contrasts with the bright areas that are mainly Galinstan LM. Due to the high temperature, the flux is carbonized, and

2365709x, 2026, 15, Downloaded from https://advanced.onlinelibrary.wiley.com/doi/10.1002/admt.202502023 by IMEC Library - IMEC , Wiley Online Library on [19/11/2026]. See the Terms and Conditions (https://onlinelibrary.wiley.com/terms-and-conditions) on Wiley Online Library for rules of use; OA articles are governed by the applicable Creative Commons License

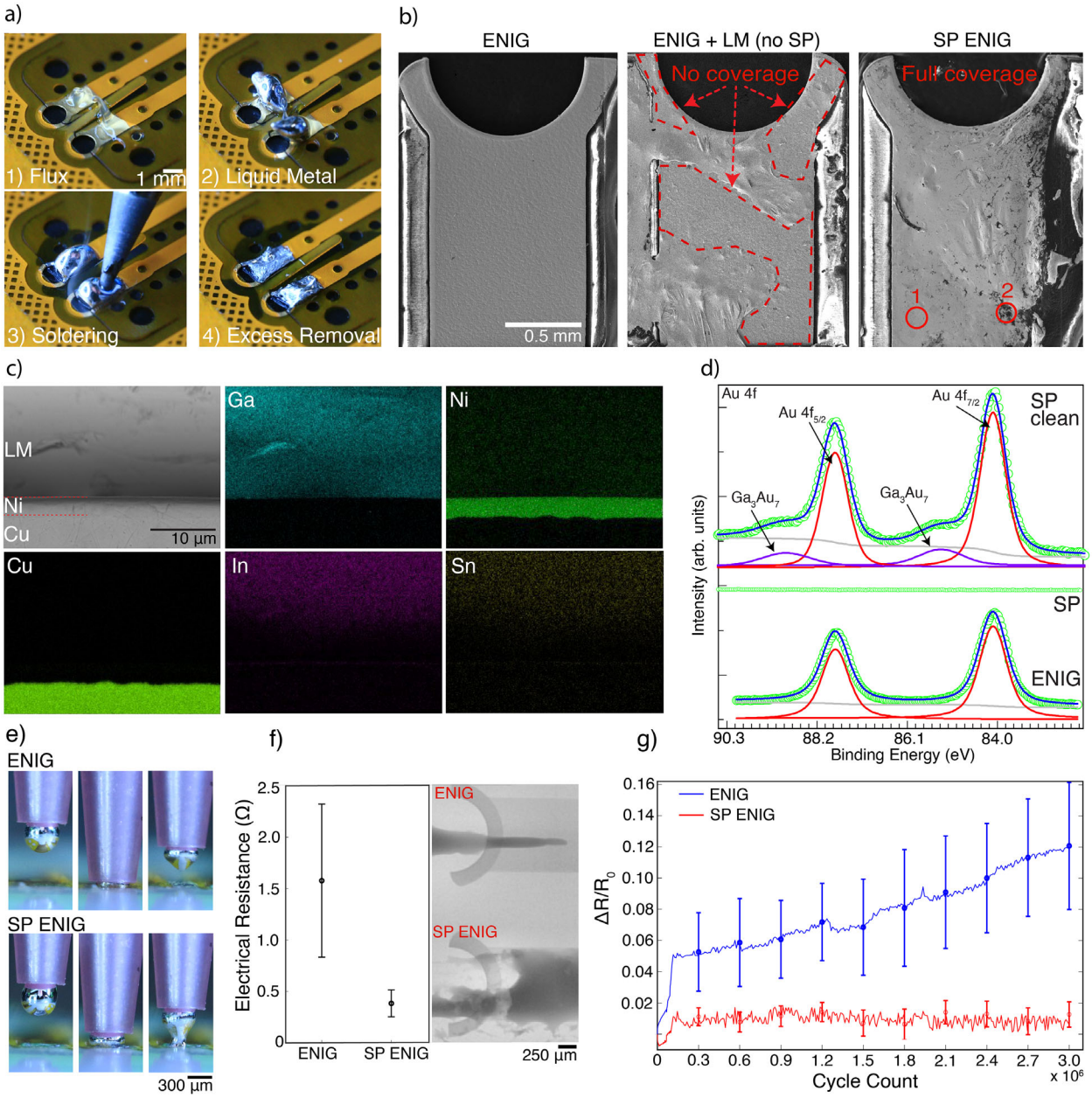


FIGURE 4 | (a) SP-process. First, flux is applied and then the LM. The LM is then soldered at 350°C onto the ENIG coating. Afterwards, excess LM is removed with a syringe. (b) SEM images of pure ENIG, ENIG, with LM that was applied without SP, and a SP electronic terminal. The SP one is fully coated in LM. (c) shows EDX mapping of a old SP-ENIG interface. The results suggest the diffusion of Ni into the LM and the depletion of in and Sn at the interface. (d) shows the Au 4f spectra of pure ENIG, cleaned ENIG-SP interface and the SP LM-air interface. The results suggest the formation of Ga_3Au_7 alloy on the cleaned interface. There is no alloying on the pure ENIG and SP-air interface. (e) On pure ENIG coating, LM does not adhere, and the meniscus even deforms rather than adhering. On the SP ENIG the LM adheres, which greatly improves printability. (f) Electrical resistance of two-terminal LMSE with pure ENIG and SP ENIG coatings. The primed coated devices have a lower initial resistance due to fully wet contact pads. (g) three million stretch cycles up to 50% strain recorded over six weeks. While pure ENIG-LM connections increase in resistance over time, devices with SP interfaces remain constant.

residue remains on the electronic terminal. However, we found that carbonization is important. Regular flux would inhibit the curing of the silicone as observed in our experiments, leading to non-functional devices. We later show that the resulting carbon residue does not compromise device stability or reliability.

To verify the formation of intermetallic compositions and elucidate the wetting behavior during the SP, cross-sectional SEM-EDX and X-ray photoelectron spectroscopy (XPS) were performed. As shown in Figure 4c, SEM-EDX mapping of the LM-ENIG SP interface reveals pronounced Ni diffusion into the LM layer, accompanied by local depletion of In and Sn near the interface. These results indicate the formation of Ga_xNi_y intermetallics directly at the solid–liquid boundary. To further confirm the formation of intermetallics, the soldered surface was cleaned immediately after the SP and examined by digital microscopy and

2365709x, 2026, 15, Downloaded from https://advanced.onlinelibrary.wiley.com/doi/10.1002/admt.202502023 by IMEC Library - IMEC , Wiley Online Library on [19/11/2026]. See the Terms and Conditions (https://onlinelibrary.wiley.com/terms-and-conditions) on Wiley Online Library for rules of use; OA articles are governed by the applicable Creative Commons License

SEM (Figure S8). The ENIG surface exhibited a distinct color change and SEM/EDX revealed the formation of intermetallic crystals, which are most likely a Ga_xNi_y alloy. Complementary XPS measurements were conducted on the cleaned SP interface, the LM-air interface, and pristine ENIG as a reference (Figure S9). The Au 4f spectra (Figure 4d) display characteristic Au $4f_{5/2}$ and Au $4f_{7/2}$ peaks in both ENIG and the cleaned SP sample. Notably, the cleaned interface shows evidence of Ga_3Au_7 formation, arising from the reaction between LM and the thin Au layer, whereas the LM-air interface exhibits no Au-related peaks. The Ga 3d spectra (Figure S10) reveal Ga(0), In, and Sn signals, together with Ga(I) and Ga(III) oxidation states, on both the cleaned interface and the LM-air surface. These findings confirm the presence of Galinstan with its native oxide layer in both cases. For the cleaned interface, this implies strong interfacial bonding between LM and ENIG, while for the LM-air interface, the surface chemistry is dominated by the LM, which governs subsequent interfacial behavior. Altogether, these results demonstrate that reactive wetting governs the SP process. It is well established that liquid metals form intermetallics with most solid metals via reactive wetting, wherein wetting is enhanced by interfacial chemical reactions [15, 34, 39]. In conventional soldering, flux removes surface oxides to enable direct metal-metal contact, and similar effects have been reported with acid treatments [40]. In the present case, Ga_3Au_7 intermetallics form between the 25 nm Au layer of ENIG and the LM, constituting the dominant phase at the solid–liquid interface. The applied soldering temperature of 350°C accelerates this interfacial reaction and lowers the LM surface tension [41, 42], thereby promoting spontaneous wetting across the substrate. Concurrently, Ni diffusion into the LM contributes to the formation of Ga_xNi_y alloys, further corroborating the intermetallic-driven wetting mechanism.

Figure 4e compares the adhesion of an LM meniscus from the nozzle on untreated ENIG versus ENIG with the SP interface. When the nozzle is lowered and then raised, no adhesion occurs on pure ENIG. The meniscus even adopts a distorted shape under pressure. In contrast, on the SP-treated surface, the LM meniscus adheres and forms a connection with the underlying layer, as evidenced by a column of LM drawn during nozzle retraction. As previously discussed, the interface is governed by Galinstan and there is high chemical affinity when stacking identical materials (LM–LM) compared to stacking foreign materials (LM–ENIG) (Figure S10)[43].

We then fabricated test devices to evaluate the electrical performance and long-term stability and reliability of the SP method. Each device consists of two 40 mm LM traces connecting our patented flex PCBs [44], encapsulated in a standardized dog-bone geometry [45]. All fabricated devices with SP interfaces (64 terminals across 20 samples) successfully printed. For untreated samples without SP interfaces the interconnection method proposed by Kim et al. was used [32]. Dragon Skin 10 is used near the flex PCBs for strain relief, while the central region is made of softer Ecoflex 30. One trace connects pure ENIG terminals, the other connects SP-treated electronic terminals.

X-ray images and resistance measurements are shown in Figure 4f. Thanks to the LM interface, traces printed on SP terminals make full contact, while traces printed on untreated ENIG are visibly thinned due to poor wetting. Consequently, SP devices exhibit 4× lower resistance and reduced variability, confirming improved and consistent mechanical contact. These values compare favorably to similar devices fabricated by DW: Kim et al. reported 1.45 Ω for similar devices (50 mm length) on pure ENIG [32]. In contrast, our SP devices reach as low as 0.38 Ω, which will significantly reduce contact noise in LMSE with solid–liquid interconnections. The results are further compared with other interconnection strategies that mainly focus on interconnecting rigid components to LM circuits (Table S1).

Finally, the devices were subjected to three million stretching cycles up to 50% strain over six weeks. The average resistance change of strained samples in the relaxed state is shown in Figure 4g. A similar trend is observed in the strained state (Figure S11). $\Delta R/R_0$ remains stable for SP devices. Due to the stable performance of the primed samples, we conclude that the remaining carbonized flux acts inertly. For non-treated samples, $\Delta R/R_0$ gradually increases at a rate of 2% per one million cycles. This suggests that the solid–liquid interface is affected by strain-related degradation, as the other parts of the LMSE are printed identically for both untreated and SP devices. Studies have reported that the conductivity of LMSE can be affected by factors such as leakage, oxidation, or delamination of the liquid–solid interface. [35, 46]. For instance, we determined empirically that there is darkening at the solid–liquid interface, which can be due to oxidation (Figure S12). Whereas SP electronic terminals are fully wet, untreated ones have a poorer contact area and lower LM volume. LMSE with untreated electronic terminals are therefore more susceptible to resistance rise due to the listed phenomena.

In conclusion, we present a SP method utilizing the reactive wetting of LM on ENIG to create a thin LM interfacial layer that significantly enhances the printability of LM on electronic terminals. It also improves electrical performance and long-term electrical stability. In the next section, we demonstrate how these improvements enable relevant applications of LM-based stretchable electronics.

2.5 | Applications

The presented advancements extend the capabilities of the DW technique, facilitating the fabrication of emerging applications. A stretchable wire is presented in Figure 5a. Straightforward in design and with countless applications in sectors that would benefit from the stretchability, softness, and robustness of a stretchable wire. For instance, as wiring in wearable electronics and smart garments, and cables in consumer electronics. The fabricated wire is 26 cm long and fabrication was only limited by the 30 by 30 cm dimensions of the print bed. Thanks to the probing and kinematic bed mesh compensation, this goes beyond the limitation of printing long traces in the order of tens of centimeters on surfaces with thickness variations and irregularities (Figure S13) [30]. This technology carries potential to upscale the DW process and enable new applications, printing on large substrates or even 3D surfaces, as demonstrated earlier.

The other major challenge is wetting issues of LM on electronic components as previously discussed. This challenge is resolved

2365709x, 2026, 15, Downloaded from https://advanced.onlinelibrary.wiley.com/doi/10.1002/admt.202502023 by IMEC Library - IMEC , Wiley Online Library on [19/11/2026]. See the Terms and Conditions (https://onlinelibrary.wiley.com/terms-and-conditions) on Wiley Online Library for rules of use; OA articles are governed by the applicable Creative Commons License

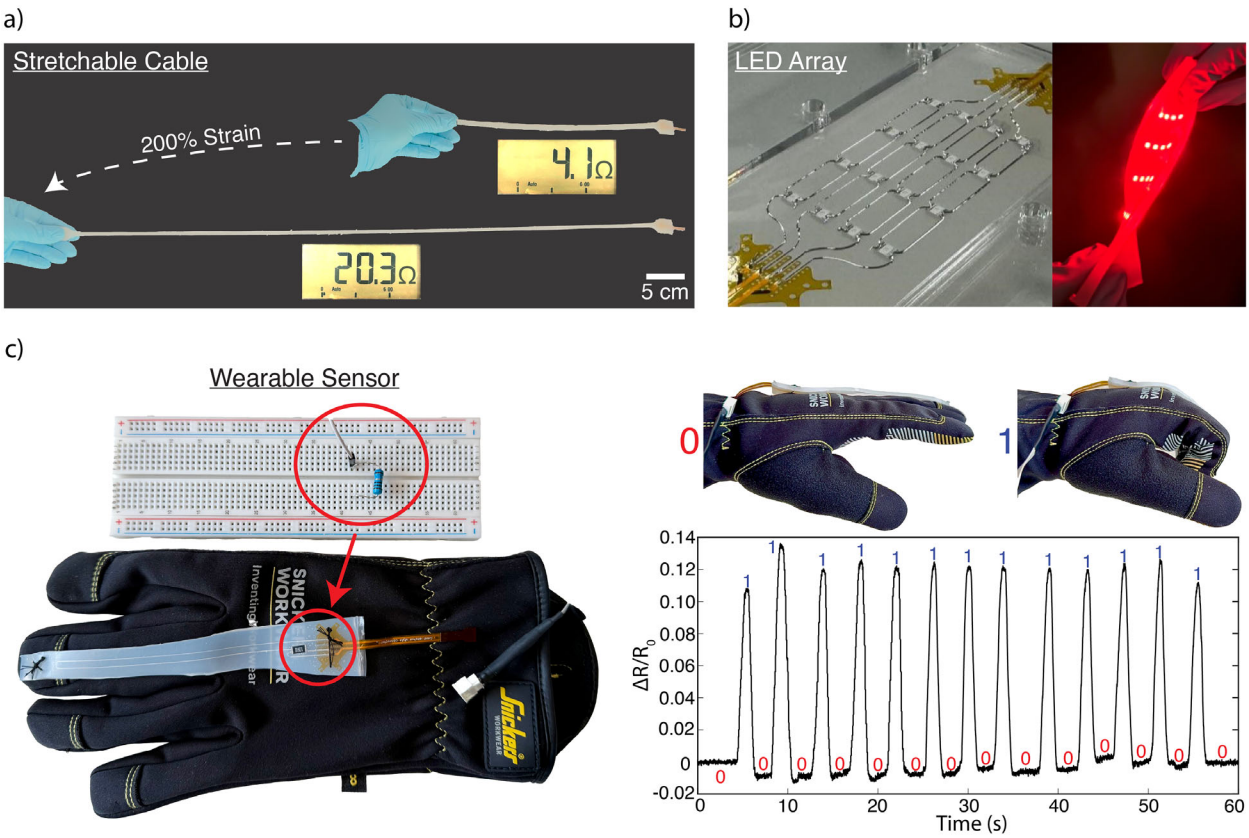


FIGURE 5 | (a) Shows a 25 cm long wire fabricated with DW utilizing the kinematic bed. The wire can easily be stretched to 75 cm in length while still working. (b) Shows a functioning 16-LED array, highlighting the capabilities of printing reliable interconnecting circuits. (c) Shows a stretchable wearable sensor that has parts of the signal processing unit directly integrated into the device. The sensor reliably captures hand movements.

with the new SP technique that creates reliable interconnections with low contact resistance. In Figure 5b, 16 LEDs are successfully interconnected with two flex PCBs, showcasing the printability on electronic components. The device works stably under stretching and twisting.

Finally, in Figure 5c, we integrated a voltage-divider circuit consisting of a resistor and multiple wires into a wearable strain sensor. This circuit is needed for signal processing and would normally require an external PCB at a minimum. With terminals of 0.5 mm in width, the integrated resistor is challenging to interconnect reliably. While the SP interconnections printed well, the non-SP interconnections would thin out or not print at all, rendering the device unusable (Figure S14). As demonstrated in the bottom-right panel, the wearable sensor with integrated electronics works well and stably (Video S3). Different hand gestures are successfully captured over time as indicated by the resistance change. The SP method advances an exciting future where electronics, including functional components and data acquisition systems, are fully and reliably integrated into stretchable devices [29, 47, 48].

3 | Conclusion

In this work, we overcome the key challenges of direct writing of liquid metal for stretchable electronics, a technique known for its precision and rapid prototyping, yet hindered by significant hurdles. These include the difficulty of printing on uneven, sloped, or curved surfaces; limited understanding of the printing dynamics; and interfacial challenges with electronic components.

To overcome these barriers, we introduced a kinematic bed system, enabling reliable printing on non-planar substrates, eliminating the reliance on ultra-flat, non-scalable spin-coated surfaces. Our system successfully prints devices over 25 cm in size and operates on slopes up to 10% and curved geometries, pushing the boundaries of substrate versatility. Additionally, the kinematic bed compensation reliably prints LM traces between 100–400 μm width.

Through systematic characterization, we discovered a pressure-driven backward flow of LM into existing traces, a time-dependent effect dependent on printing velocity and nozzle-to-substrate distance. This insight provides a critical understanding of the dynamics that govern print geometry, enabling tuning of trace thickness in a range of 100 μm.

To address the persistent challenge of unreliable printing and poor contact with electronic terminals, we developed a solder-priming method utilizing the reactive wetting of LM on ENIG to create a thin LM interfacial layer that enables LM adhesion on electronic terminals, achieving 100% printing reliability. Further, SP interconnections reduce contact resistance by 4× through electronic terminals fully wet with LM. SP devices maintain stable electrical performance over three million stretching cycles,

2365709x, 2026, 15, Downloaded from https://advanced.onlinelibrary.wiley.com/doi/10.1002/admt.202502023 by IMEC Library - IMEC , Wiley Online Library on [19/11/2026]. See the Terms and Conditions (https://onlinelibrary.wiley.com/terms-and-conditions) on Wiley Online Library for rules of use; OA articles are governed by the applicable Creative Commons License

whereas non-primed counterparts show progressive degradation. With relevant applications, such as a 26 cm long wire and a wearable sensor with integrated electronics, we demonstrated the advancements presented in this article.

By solving key challenges, this work enables printing on sloped and large surfaces, the seamless integration of rigid electronics into liquid metal-based soft systems, and provides new insights into the technique. These advances not only extend the applicability of LM DW but also bring us closer to fully integrated, high-performance stretchable electronics.

4 | Experimental Section

4.1 | Materials

Galinstan, a Gallium–Indium–Tin alloy, was used as the liquid conductor, with a composition of Ga = 65–95 wt.%, In = 5–22 wt.%, and Sn = 0–11 wt.% (Polymet). The silicone elastomer Ecoflex 30 and Dragon Skin 10 (Smooth-On, FormX) was employed as the stretchable encapsulation material. We used NC-559-V2-TF solder flux for the solder priming. We used Nordson SmoothFlow tapered tips and PTFE coated tips with an inner diameter of 0.56 and 0.25 mm, respectively, for printing. The custom-designed and patented flex PCB for the device interconnections were fabricated from polyamide (PI) and polyethylene terephthalate (PET) with ENIG-plated copper pads and ordered from JLPCB. The resistors and LEDs are Sn RS PRO 10 Ω, 2512 (6432M) and Ag plated Broadcom 2.6 V Super Red LED; respectively, and ordered from RS. Cu pieces and evaporated Au on glas were used. To clean the electronic terminals off LM, Simple Green cleaner was applied to the terminal and LM was gently wiped away. Afterwards, the area was rinsed with DI water and blown dry with a nitrogen gun.

4.2 | Direct Writing System

The direct writing system is based on a RatRig core 3.1 3D printer with customized parts for syringe, print bed, and enclosure. An Antclabs BLTouch 3.1 was used for homing as well as surface probing. The RatRig printer runs with RatOS, and the underlying software that controls the motions is Klipper. The bed mesh was a defined squared area. To generate the bed mesh, the number of probed points in X and Y direction, as well as the range are defined in the configuration file of RatOS. The system can then automatically probe and record the surface according to the input to generate the mesh. Before any print-start, the mesh was loaded to enable bed mesh compensation, which was handled by Klipper. The syringe setup was fully acquired from Nordson, where we used the Ultimus V as a pressure controller and an EFD syringe with a blue piston. An Arduino setup connected to both printer and pressure controller lets us control the applied pressure during printing with GCode.

4.3 | COMSOL Model

Uniaxial strain tests of the Ecoflex and Dragon Skin were performed using a dynamic mechanical analysis (DMA, RSA-G2 TA Instruments) machine. The Mooney-Rivlin parameters for Ecoflex and Dragon Skin were C10 = 31311 Pa, C01 = −7503.8 and C10 = 64820 Pa, C01 = −11041 Pa, respectively. The tip of the BLTouch was visualized and measured with a Keyence VHX-5000, and the tip diameter was approximately 0.5 mm. The force of the BLTouch during probing was measured with a Vernier force sensor and is approximately 11 mN. The simulation was swept in a substrate thickness range between 0.4 and 2.6 mm. The model was validated by fabricating slabs of silicone with different thicknesses, which were measured with a Gauge Probe. The printer was then homed on the slabs, and we determined the thickness offset once the nozzle left no visible dent anymore when increasing the z height in steps of 5 μm.

4.4 | Solder Priming

The solder priming process starts with clean electronic terminals before the actual printing step. First, solder flux was applied onto the coatings. A small blob within the boundaries of the terminal was sufficient. With a micro syringe, few μL of LM were applied onto the terminals. Excessive LM should already be removed so as not to short the electronic terminals during the soldering process. The LM was now soldered with a standard non-contaminated soldering iron at 350°C for a second. The LM should fully wet the electronic terminal on its own. Finally, excessive bulk LM was removed to create the thin interfacial layer.

4.5 | Printing Parameters

For the 0.56 mm inner diameter tips, we found that the most influential parameters on the printing were SOD, relative humidity, and applied pressure. The total pressure at the nozzle tip is the difference between hydrostatic pressure in the syringe and the applied vacuum [30]:

$$P = P_h + P_v = \rho_{GaInSn} * g * h + P_v \tag{2}$$

where P_h is the hydrostatic pressure of the Galinstan at the nozzle tip, P_h is the applied vacuum (negative pressure), ρ_{GaInSn} is the density of Galinstan, g is the earth gravity acceleration and h is vertical distance between the nozzle tip and the fill level of the LM. Humidity was kept between 36–44%, consistent with the printable range reported in literature [30]. For pressures above 1.85 kPa, LM often bursts through the oxide, resulting in uncontrolled spreading. For pressures below 0.85 kPa, the meniscus radius was too small to reliably contact the surface. Although printing at velocities ≥65 mm s^{-1} was feasible, we used a velocity of 6.5 mm s^{-1} to reduce vibration-induced edge roughness (Figure S5, Supporting Information) Velocity during initial contact and nozzle lifting is 2 mm s^{-1} to avoid spilling. For the 0.25 mm nozzle, pressure was increased to 4 kPa to accommodate for the smaller meniscus.

4.6 | LMSE Fabrication

The fabrication process begins with four laser-cut acrylic plates for a single-layer device: a baseplate, an injection plate, and

2365709x, 2026, 15, Downloaded from https://advanced.onlinelibrary.wiley.com/doi/10.1002/admt.202502023 by IMEC Library - IMEC , Wiley Online Library on [19/11/2026]. See the Terms and Conditions (https://onlinelibrary.wiley.com/terms-and-conditions) on Wiley Online Library for rules of use; OA articles are governed by the applicable Creative Commons License

1st and 2nd cutout plates. First, the flex PCB (and any rigid components) were glued onto the engraved baseplate using a light, water-soluble glue, with the bond pads facing down. The components were then sprayed with silicone adhesion primer (Wacker G790, toluene-free) and left to cure under ambient conditions for 1.5 h. The two-component silicone was mixed in a 50:50 ratio using a speedmixer (Hauschild) and degassed for 20 min. First, a small blob of stiff Dragon Skin ten was put around the components. Then, softer Ecoflex 30 is injected into the baseplate–1st cutout–injection plate stack and cured in a 50°C oven for 30 min. Afterward, the substrate was released and flipped. The electrical components were now solder primed. After waiting period of at least 45 min after taking the samples from the oven, which was necessary for the probe measurements to stabilize, the substrates were probed with the BLTouch for bed meshing (Figure S15). The probing grid depends on the size and complexity of the device. For the small dogbone samples, a 5 by 5 grid was sufficient. For the strain sensor, we used a 7 by 10 grid. The devices are then patterned via DW. Finally, a second cutout is placed on top of the samples and the encapsulation was carefully plate-coated, where a blob of Dragon Skin 10 was again placed around the components. The samples are cured again for 30 min in the oven.

4.7 | Characterization

The bulk elemental composition of the coatings was characterized using SEM-EDX (JEOL JSM-IT300). An accelerating voltage of 15 keV was used with a working distance of 10 mm. The chemical composition was obtained with EDX. The quantification was performed using the manufacturer provided sensitivity factors, and the values were obtained for a relative comparison between the points. XPS was carried out using a standalone HAXPES-lab system from Scienta Omicron. Two monochromatized X-ray sources were available: a gallium Kα line (9251.63 eV, full width at half maximum = 0.45 eV) and an aluminium Kα line (1 486.7 eV, FWHM = 0.25 eV). The binding-energy scale was calibrated with a clean Au substrate, setting the Au $4f_{7/2}$ core-level peak to 84.0 eV. Geometrical properties of printed traces were characterized using a Keyence VHX-5000 digital microscope and analyzed with Keyence software. The bulk resistance of the devices was measured using a Keithley 2400 source meter with four-wire measurements. Cycle testing was performed using in-house cycle testers. The testers were connected to the source meter and multiplexer, recording temperature, pressure, and humidity. The electronic terminal connections were visualized with X-Ray YXLON Cheetah EVO. High-quality images and videos were captured using a Canon EOS 70D camera with a Laowa 100 mm Ultra-Macro lens. For motion sensing applications, the sensor was integrated into a glove and motion was captured using an Arduino.

Author Contributions

Maximilian Krack: Conceptualization, investigation, data curation, methodology, formal analysis, and draft writing; **Lennert Purnal**: Investigation (Dynamic pressure control; Figure 4 cycle testing); **Parth Vinayakrao Sewlikar**: Investigation (SEM/EDX); **Sam Cuyvers**: Investigation (Building the core direct writing system) **Gus Geurts**: Investigation (Building the core direct writing system) **Rathul Nengminza Sangma**: Investigation (Figure 5c sensor design and characterization); **Derese Desta**: Investigation (XPS), data curation (XPS); **Dieter Reenaers**: Investigation (Figures 3 and 4 camera images and videos); **Bart Ruttens**: Investigation (X-Ray); **Iris De Graeve**: Supervision; **Tom Hauffman**: Supervision; **Seppe Terryn**: Supervision; **Bram Vanderborght**: Supervision; **Michaël Daenen**: Supervision; **Wim Deferme**: Supervision, review and editing, funding acquisition, project administration; **Monika Rai**: Supervision, formal analysis and review and editing of the original draft.

Acknowledgements

The authors want to thank the funding organizations for their crucial contribution to enable this research work. This includes the personal funding for Maximilian Krack provided by the Fonds Wetenschappelijk Onderzoek (FWO, 1SH1C24N), as well as the supporting bench fee provided by the Bijzonder Onderzoeksfonds (BOF, BOF23INCENT17). The author also thank FWO for providing funding within the broader SBO project of SUBLIME (S007423N), enabling a research network across a wide range of faculties.

Conflicts of Interest

The authors declare no conflicts of interest.

Data Availability Statement

The data that support the findings of this study are available from the corresponding author upon reasonable request.

References

1. S. Zhu, J.-H. So, R. Mays, et al., "Ultrastretchable Fibers With Metallic Conductivity Using a Liquid Metal Alloy Core," *Advanced Functional Materials* 23, no. 18 (2013): 2308–2314.

2. D. Qi, K. Zhang, G. Tian, B. Jiang, and Y. Huang, "Stretchable Electronics Based on PDMS Substrates," *Advanced Materials* 33, no. 6 (2021): 2003155.

3. W. Wu, "Stretchable Electronics: Functional Materials, Fabrication Strategies and Applications," *Science and Technology of Advanced Materials* 20, no. 1 (2019): 187–224.

4. J. F. Elfferich, D. Dodou, and C. Della Santina, "Soft Robotic Grippers for Crop Handling or Harvesting: A Review," *IEEE Access* 10 (2022): 75428–75443.

5. E. Palleau, S. Reece, S. C. Desai, M. E. Smith, and M. D. Dickey, "Self-Healing Stretchable Wires for Reconfigurable Circuit Wiring and 3D Microfluidics," *Advanced Materials* 25, no. 11 (2013): 1589–1592.

6. Y.-G. Park, G.-Y. Lee, J. Jang, S. M. Yun, E. Kim, and J.-U. Park, "Liquid Metal-Based Soft Electronics for Wearable Healthcare," *Advanced Healthcare Materials* 10, no. 17 (2021): 2002280.

7. J. Shintake, V. Cacucciolo, D. Floreano, and H. Shea, "Soft Robotic Grippers," *Advanced Materials* 30, no. 29 (2018): 1707035.

8. R. N. Sangma, S. Terryn, M. Krack, et al., "Recyclable and Self-Healing Stretchable Strain Sensor Based on Liquid Metal and Diels-Alder Polymer for Smart Wearable Applications," *IEEE Sensors Journal* (2025).

9. T. Liu, P. Sen, and C.-J. Kim, "Characterization of Nontoxic Liquid-Metal Alloy Galinstan for Applications in Microdevices," *Journal of Microelectromechanical Systems* 21, no. 2 (2011): 443–450.

10. K. Foremny, S. Nagels, M. Kreienmeyer, T. Doll, and W. Deferme, "Biocompatibility Testing of Liquid Metal as an Interconnection Material for Flexible Implant Technology," *Nanomaterials* 11, no. 12 (2021): 3251.

11. J. Qin, D. Cui, L. Ren, W. Hao, Y. Shi, and Y. Du, "Emerging Advances of Liquid Metal Toward Flexible Sensors," *Advanced Materials Technologies* 9, no. 14 (2024): 2300431.

2365709x, 2026, 15, Downloaded from https://advanced.onlinelibrary.wiley.com/doi/10.1002/admt.202502023 by IMEC Library - IMEC , Wiley Online Library on [19/11/2026]. See the Terms and Conditions (https://onlinelibrary.wiley.com/terms-and-conditions) on Wiley Online Library for rules of use; OA articles are governed by the applicable Creative Commons License

12. Z. Xue, T. Dong, Z. Zhu, Y. Zhao, Y. Sun, and L. Yu, "Engineering In-Plane Silicon Nanowire Springs for Highly Stretchable Electronics," *Journal of Semiconductors* 39, no. 1 (2018): 011001.

13. E. Roels, S. Terryn, J. Brancart, F. Sahraeeazartamar, F. Clemens, G. Van Assche, and B. Vanderborght, "Self-Healing Sensorized Soft Robots," *Materials Today Electronics* 1 (2022): 100003.

14. S. Nagels and W. Deferme, "Fabrication Approaches to Interconnect Based Devices for Stretchable Electronics: A Review," *Materials* 11, no. 3 (2018): 375.

15. S.-Y. Tang, C. Tabor, K. Kalantar-Zadeh, and M. D. Dickey, "Gallium Liquid Metal: The Devil's Elixir," *Annual Review of Materials Research* 51, no. 1 (2021): 381–408.

16. M. D. Dickey, "Emerging Applications of Liquid Metals Featuring Surface Oxides," *ACS Applied Materials & Interfaces* 6, no. 21 (2014): 18369–18379.

17. L. Purnal, M. Rai, S. Vandervoort, M. Kellens, B. Claessen, J. Nivelle, S. Nagels, M. Daenen, and W. Deferme, "Influence of Uniaxial Stretching on the Joule Effect-Induced Heating of Liquid Metal-Based Stretchable Electronic Devices," (2025): 234–241.

18. L. Zhu, B. Wang, S. Handschuh-Wang, and X. Zhou, "Liquid Metal-Based Soft Microfluidics," *Small* 16, no. 9 (2020): 1903841.

19. B. Wang and A. Facchetti, "Mechanically Flexible Conductors for Stretchable and Wearable E-Skin and E-Textile Devices," *Advanced Materials* 31, no. 28 (2019): 1901408.

20. G. Li, F. Sun, H. Chen, Y. Jin, A. Zhang, and J. Du, "High-Efficiency Large-Area Printed Multilayer Liquid Metal Wires for Stretchable Biomedical Sensors With Recyclability," *ACS Applied Materials & Interfaces* 13, no. 48 (2021): 56961–56971.

21. F. Sahraeeazartamar, S. Terryn, R. N. Sangma, et al., "Diels-Alder Network Blends as Self-Healing Encapsulants for Liquid Metal-Based Stretchable Electronics," *ACS Applied Materials & Interfaces* 16, no. 26 (2024): 34192–34212.

22. N. Lazarus, S. S. Bedair, and I. M. Kierzewski, "Ultrafine Pitch Stencil Printing of Liquid Metal Alloys," *ACS Applied Materials & Interfaces* 9, no. 2 (2017): 1178–1182.

23. L. Wang and J. Liu, "Pressured Liquid Metal Screen Printing for Rapid Manufacture of High Resolution Electronic Patterns," *RSC Advances* 5, no. 71 (2015): 57686–57691.

24. Y. Lin, O. Gordon, M. R. Khan, N. Vasquez, J. Genzer, and M. D. Dickey, "Vacuum Filling of Complex Microchannels With Liquid Metal," *Lab on a Chip* 17, no. 18 (2017): 3043–3050.

25. H.-Y. Chen and A. T. Conn, "A Stretchable Inductor With Integrated Strain Sensing and Wireless Signal Transfer," *IEEE Sensors Journal* 20, no. 13 (2020): 7384–7391.

26. T. V. Neumann and M. D. Dickey, "Liquid Metal Direct Write and 3D Printing: A Review," *Advanced Materials Technologies* 5, no. 9 (2020): 2000070.

27. Y. Yoon, S. Kim, D. Kim, S. K. Kauh, and J. Lee, "Four Degrees-of-Freedom Direct Writing of Liquid Metal Patterns on Uneven Surfaces," *Advanced Materials Technologies* 4, no. 2 (2019): 1800379.

28. J. W. Boley, E. L. White, G. T.-C. Chiu, and R. K. Kramer, "Direct Writing of Gallium-Indium Alloy for Stretchable Electronics," *Advanced Functional Materials* 24, no. 23 (2014): 3501–3507.

29. J. Ma, F. Krisnadi, M. H. Vong, M. Kong, O. M. Awartani, and M. D. Dickey, "Shaping a Soft Future: Patterning Liquid Metals," *Advanced Materials* 35, no. 19 (2023): 2205196.

30. A. Cook, D. P. Parekh, C. Ladd, et al., "Shear-Driven Direct-Write Printing of Room-Temperature Gallium-Based Liquid Metal Alloys," *Advanced Engineering Materials* 21, no. 11 (2019): 1900400.

31. S. Kim, J. Oh, D. Jeong, W. Park, and J. Bae, "Consistent and Reproducible Direct Ink Writing of Eutectic Gallium-Indium for High-Quality Soft Sensors," *Soft Robotics* 5, no. 5 (2018): 601–612.

32. S. Kim, J. Oh, D. Jeong, and J. Bae, "Direct Wiring of Eutectic Gallium-Indium to a Metal Electrode for Soft Sensor Systems," *ACS Applied Materials & Interfaces* 11, no. 22 (2019): 20557–20565.

33. Z. Zou, Y. Chen, S. Yuan, N. Luo, J. Li, and Y. He, "3D Printing of Liquid Metals: Recent Advancements and Challenges," *Advanced Functional Materials* 33, no. 10 (2023): 2213312.

34. J.-H. Kim, S. Kim, M. D. Dickey, J.-H. So, and H.-J. Koo, "Interface of Gallium-Based Liquid Metals: Oxide Skin, Wetting, and Applications," *Nanoscale Horizons* 9, no. 7 (2024): 1099–1119.

35. M. Krack, R. N. Sangma, L. Purnal, et al., "Process and property assessment of liquid metal spray deposition towards scalable and reliable stretchable electronics," *Scientific Reports* 15, no. 1 (2025): 35984.

36. C. Wan, Y. Liu, X. Li, H. Xu, R. Guo, and J. Liu, "Interfacial Adhesion Effects of Liquid Metal Printed Electronics on General Substrates: Mechanisms and Applications," *InfoMat* (2025): e70029.

37. T. M. Squires and S. R. Quake, "Microfluidics: Fluid Physics at the Nanoliter Scale," *Reviews of Modern Physics* 77, no. 3 (2005): 977–1026.

38. S. Orgeig, W. Bernhard, S. C. Biswas, et al., "The Anatomy, Physics, and Physiology of Gas Exchange Surfaces: Is There a Universal Function for Pulmonary Surfactant in Animal Respiratory Structures?" *Integrative and Comparative Biology* 47, no. 4 (2007): 610–627.

39. W. Lin, W. Qiu, Y. Tuersun, X. Huang, and S. Chu, "Ultrastrong Spontaneous Surface Wetting of Room Temperature Liquid Metal on Treated Metal Surface," *Advanced Materials Interfaces* 8, no. 18 (2021): 2100819.

40. J. Tang, X. Zhao, J. Li, Y. Zhou, and J. Liu, "Liquid Metal Phagocytosis: Intermetallic Wetting Induced Particle Internalization," *Advanced Science* 4, no. 5 (2017): 1700024.

41. A. Rasouli, A. Kudyba, G. Bruzda, J. Safarian, and G. Tranell, "High-Temperature Reactive Wetting of Natural Quartz by Liquid Magnesium," *Materials* 17, no. 6 (2024): 1302.

42. Y. Plevachuk, V. Sklyarchuk, S. Eckert, G. Gerbeth, and R. Novakovic, "Thermophysical Properties of the Liquid Ga-In-Sn Eutectic Alloy," *Journal of Chemical & Engineering Data* 59, no. 3 (2014): 757–763.

43. C. Ladd, J.-H. So, J. Muth, and M. D. Dickey, "3D Printing of Free Standing Liquid Metal Microstructures," *Advanced Materials* 25, no. 36 (2013): 5081–5085.

44. Interconnect, an electronic assembly and a method for manufacturing an electronic assembly, author = Steven Nagels, Thijs Vandenryt, Wim Deferme, ep = EP21185696.8A, year = 2021.

45. "Plastics — determination of tensile properties, part 1," 2019.

46. S. Lee, J. Ma, Y. Hioki, et al., "Practical Considerations for Gallium-Based Liquid Metal for Stretchable Electronics: Metal Contacts and Strain Cycling," *ACS Applied Electronic Materials* (2025).

47. Z. Lin, T. Li, S. Yang, B. Ji, and Z. Wang, "Revolutionizing Flexible Electronics With Liquid Metal Innovations," *Device* 2, no. 5 (2024).

48. S. Xu, Y. Zhang, L. Jia, et al., "Soft Microfluidic Assemblies of Sensors, Circuits, and Radios for the Skin," *Science* 344, no. 6179 (2014): 70–74.

Supporting Information

Additional supporting information can be found online in the Supporting Information section.

Supporting Information: admt70624-sup-0001-SuppMat.pdf

Supporting Information: Supplemental Video 1

Supporting Information: Supplemental Video 2

Supporting Information: Supplemental Video 3

2365709x, 2026, 15, Downloaded from https://advanced.onlinelibrary.wiley.com/doi/10.1002/admt.202502023 by IMEC Library - IMEC , Wiley Online Library on [19/11/2026]. See the Terms and Conditions (https://onlinelibrary.wiley.com/terms-and-conditions) on Wiley Online Library for rules of use; OA articles are governed by the applicable Creative Commons License